Journal of Nuclear Materials 454 (2014) 114–118

Contents lists available at ScienceDirect

Journal of Nuclear Materials

journal homepage: www.elsevier.com/locate/jnucmat

Influence of TiN nanoparticles on the microstructure and properties of W matrix materials prepared by spark plasma sintering

Shuang Wang [a], Lai-Ma Luo [a,c,*], Xiao-Yue Tan [a], Guang-Nan Luo [b], Xiang Zan [a,c], Ji-Gui Cheng [a,c], Xiao-Yong Zhu [a,c], Yu-Cheng Wu [a,c,*]

[a] School of Materials Science and Engineering, Hefei University of Technology, Hefei 230009, China
[b] Institute of Plasma Physics, Chinese Academy of Sciences, Hefei 230031, China
[c] Engineering Research Center of Powder Metallurgy of Anhui Province, Hefei 230009, China

HIGHLIGHTS

- Effect of TiN on microstructure and properties of composites were studied.
- TiN particles exist in the grain interior and at the grain boundary.
- The tensile strength reached 180 MPa when the content of TiN was 2 wt.%.

ARTICLE INFO

Article history:
Received 21 May 2014
Accepted 24 July 2014
Available online 4 August 2014

ABSTRACT

W–(0.5, 1, 2, 4) wt.% TiN composite powders were formed by mechanical alloying for 5 h and sintered by spark plasma at 1800 °C. The effect of TiN nanoparticle content on the microstructure and properties of the composites were investigated by scanning electron microscopy, transmission electron microscopy, tensile test, microhardness test, and thermal conductivity test. With the addition of TiN ranging from 0.5 wt.% to 4 wt.%, SEM analysis results showed that TiN was distributed homogeneously and W grains were refined by TiN. The fracturing of pure W was intergranular, whereas cleavage fracture appeared in the W–TiN composites and increased with increased TiN content. The density was found to initially increase and then decrease with increased TiN content. The same trend was observed for the thermal conductivity. Microhardness increased with increased TiN content. The tensile strength reached 180 MPa when the content of TiN was 2 wt.%. Furthermore, the mechanical properties of 2 wt.% exceeded those of other alloys at different TiN weight percentages.

1. Introduction

Tungsten (W) is considered to have highly promising use in plasma facing materials exposed to irradiation environments because of their high melting points, low thermal expansion coefficients, low tritium retention, and low sputtering yield [1–3]. However, these materials are known to exhibit serious embrittlement in several regimes, including low temperature, recrystallization, and radiation embrittlement, which limits the structural applications of W materials [4–6]. Solution and dispersion strengthening methods of W matrix materials are expected to solve the problems by refining the grains, lowering the DBTT, and enhancing the mechanical properties, which can be achieved by the addition of a second phase [7–9]. W alloys with certain dispersed oxides, such as La_2O_3 and Y_2O_3, as well as carbides, such as TiC and ZrC have been reported in the previous work [10–12]. The strengthening of the W matrix with nitrides such as TiN by mechanical alloying is another promising method which has never been reported. Titanium nitride is a hard refractory material with high melting point, high thermal shock resistance, low density, and abrasion resistance [13–15].

The recrystallization temperature of pure tungsten is known to be about 1200 °C [16], and the conventional sintering of tungsten is carried out at temperatures as high as 2200 °C to obtain fully dense tungsten. Naturally, the grain may be coarsened, leading to the decrease in mechanical properties. Spark plasma sintering (SPS) has been applied in the present work. Compared to conventional sintering, SPS alloys the powder materials to fine grain and high density at a relatively low temperature and with rapid heating and cooling rates [17–19].

* Corresponding authors at: School of Materials Science and Engineering, Hefei University of Technology, Hefei 230009, China. Tel./fax: +86 551 62901012.
E-mail address: luolaima@126.com (L.-M. Luo).

http://dx.doi.org/10.1016/j.jnucmat.2014.07.057
0022-3115/

In this work a W matrix reinforced by TiN nanoparticles was fabricated through spark plasma sintering, and the effect of these nanoparticles on the microstructure and properties of W matrix materials was investigated.

2. Experimental procedures

TiN powder with a grain diameter of 20–100 nm was utilized. W powder with a grain diameter of 1.0 μm to 1.3 μm (produced by Xiamen Golden Egret Special Alloy Co., Ltd.) was used. Powders were milled in a planetary mill for 5 h. A ball-to-powder weight ratio of 10:1 and a rotation speed of 400 rpm were adopted. The consolidation of the samples was carried out through SPS (SE-607, Germany) technique. The temperature and pressure profile of the sintering program in this study is illustrated in Fig. 1. First, the as-prepared powders were loaded into a graphite mold. For easy demolding, graphite papers were placed between the as-prepared powders and punch. Second, a uniaxial pressure from 3 kN to 15 kN was applied, while the powders were heated by pulse current to 450 °C. Then, the pressure was increased to 18 kN, and the powders were heated to 600 °C with a heating rate of approximately 100 °C/min under this constant pressure. The powders were maintained at 600 °C for 3 min to keep the stress uniform. Afterward, the powders were maintained at 900 °C for 6 min so the TiN could disperse uniformly. Finally, the sample was heated at 1800 °C for 1.5 min, and then cooled down with a cooling rate of 100 °C/min. These sintering processes were conducted in Ar + 3% H_2 atmosphere. Four samples were prepared by spark plasma sintering following the same sintering program. The size of the sintered samples was measured to be approximately 20 mm in diameter and 2.5 mm in thickness.

Then, the SPS sintered samples were machined by Wire cut Electrical Discharge Machining (WEDM). The relative density of the sintered samples was determined using Archimedes principle. After milling, the powders were characterized by X-ray diffraction (XRD) and field emission scanning electron microscope (FE-SEM). Fracture surfaces were examined with FE-SEM and energy dispersion spectroscopy (EDS). The microstructure was observed using transmission electron microscopy (TEM), and TEM observations were made using a JEM-2100 FX. Vickers microhardness was measured at room temperature with a load of 200 gf for 10 s. The tensile test was performed using Instron 5967 test machine at the temperature of 200 °C with a constant strain rate of 0.05 mm/s. The thermal diffusion coefficient was measured by laser thermal conductivity meter (LFA 457).

3. Results and discussion

3.1. Characterization of milling powders

The XRD pattern of the W–0.5 wt.% TiN composite powders milled for 5 h is presented in Fig. 2. As can be seen in the figure, the four main peaks were attributed to W. The TiN peak cannot be detected, possibly because of its small amount.

The SEM micrographs of the ball-milled W–TiN powders are presented in Fig. 3. Pure W particles are known to be smooth and have a nearly spherical structure. As shown in Fig. 3, the W–TiN powders after milling are work hardened and fractured by fragmentation, exhibiting large irregular shapes with a particle size of 0.5–1 μm. The powders were refined by MA and exhibited a certain degree of aggregation. The powders accumulated considerable distortional, strain, and surface energies, which reduced the activation energy of the composite sintering process and increased the activity sintering of the composite powders, as well as promoted the densification of the powders at a relatively lower temperature.

3.2. Characterization of sintering samples

3.2.1. Basic mechanical properties

The density of W–TiN composites was measured using Archimedes principle. The density of the composites was seen to increase first and subsequently decreased with the increase in TiN content. The alloy with 2 wt.% TiN had the highest relative density at 98.73%, whereas the 4 wt.% TiN alloy had the lowest, which was 97.8%. These results indicate that the addition of the appropriate amount of TiN was beneficial in consolidating W powder sintering. At the content of 4 wt.%, however, the density descended because more TiN, which has a lower density than W, existed at the W grain boundary, which prevented the migration of W during sintering.

The microhardness of W–TiN of varying content was 774.7, 688.3, 855.7, and 958.9 Hv, as shown in Fig. 4. Microhardness exhibited an increasing trend with the addition of TiN, which could be attributed to high hardness of the second phase TiN. At 4 wt.% TiN, the decrease of density did not result in a decline of hardness.

The measured tensile strength and elastic modulus are shown in Table 1, which can explain the dependence of fracture strength and the elastic modulus of the W–TiN composites on the addition of TiN. The ultimate tensile strength increased with the addition of TiN up to 2 wt.% from 136 MPa to 180 MPa, a 30% increase. When the addition of TiN was increased from 2 wt.% to 4 wt.%, the tensile

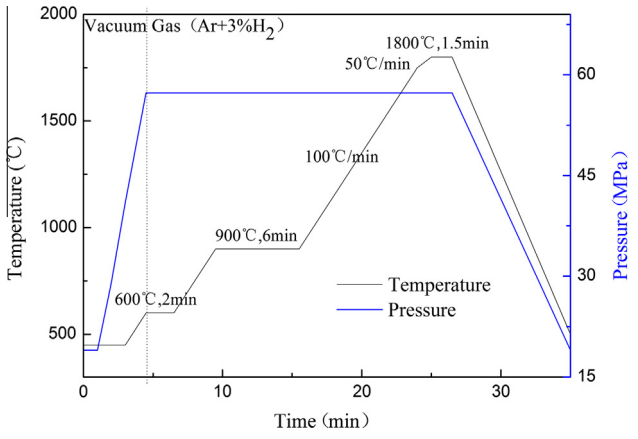

Fig. 1. Temperature and pressure profile of SPS process for the W–TiN.

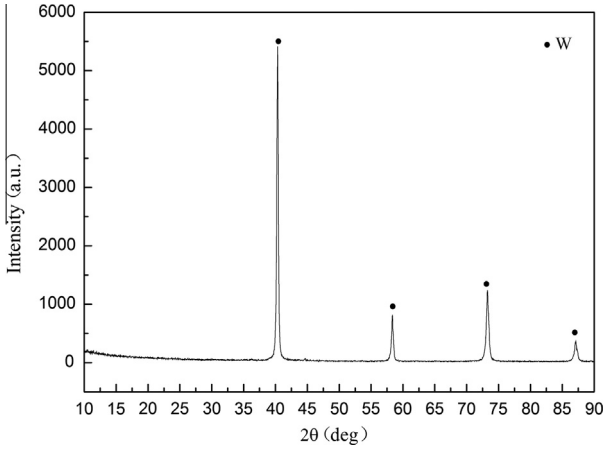

Fig. 2. The XRD pattern of W–0.5 wt.% TiN composite powder for ball-milling 5 h.

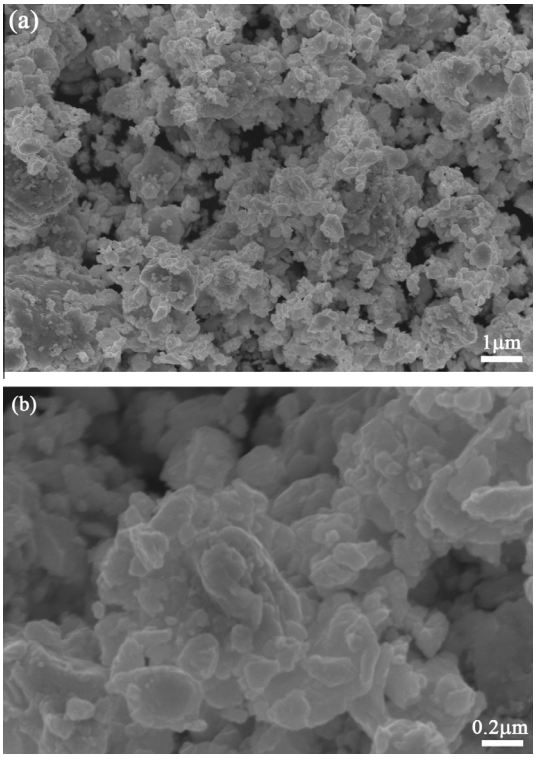

Fig. 3. SEM photographs of the ball-milled W–TiN powders.

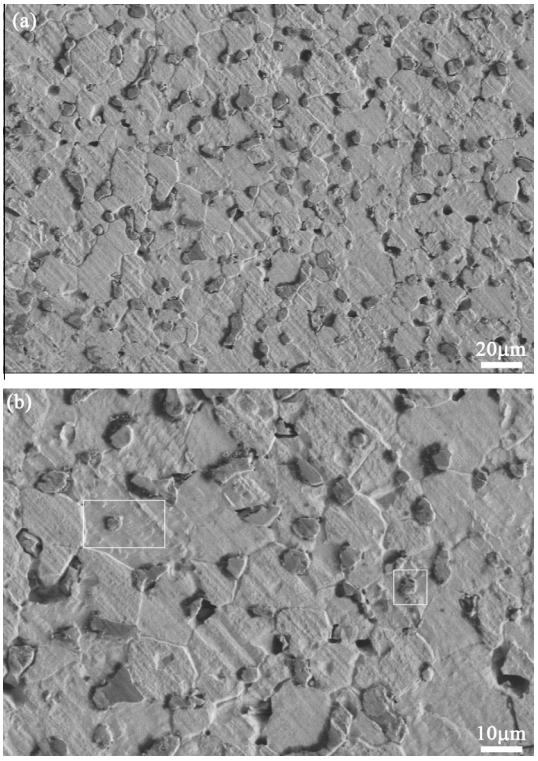

Fig. 5. SEM and EDS micrograph of the surface of W–0.5 wt.% TiN composite.

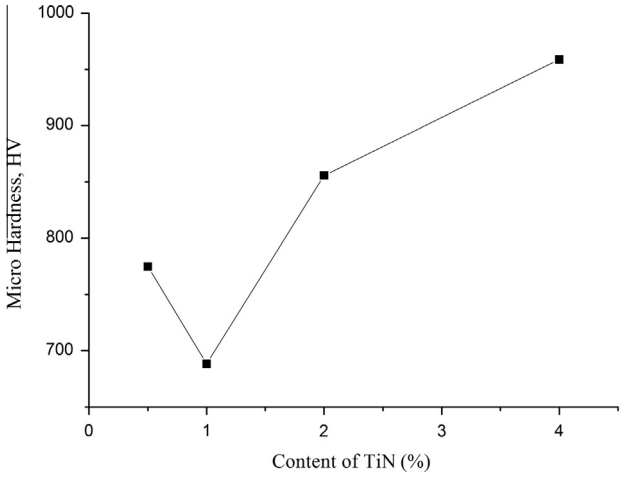

Fig. 4. Micro-hardness investigated of W–TiN composites.

Table 1
Tensile strength and elastic modulus of W–TiN composites at 200 °C.

Samples	Temperature (°C)	Ultimate tensile (MPa)	Elastic modulus
W–0.5 wt.% TiN	200	104	6192
W–1 wt.% TiN	200	136	7189
W–2 wt.% TiN	200	180	16,322
W–4 wt.% TiN	200	158	13,954

strength decreased from 180 MPa to 158 MPa. This trend could be attributed to the density of W–4 wt.% TiN being lower than that of 2 wt.%. The elastic modulus reached a maximum of 16,332 MPa for W–2 wt.% TiN.

3.2.2. Microstructure characterization

The surface image of composites is displayed in Fig. 5. EDS results revealed that the dark gray phase was Ti-rich region, while the light gray region was the W matrix. The second phase appears to be homogeneously distributed in the W matrix. TiN is seen to be mainly distributed at the grain boundaries, and only a small amount was present in the grain interior, which could hinder the grain growth by pinning effect.

Fig. 6 shows the SEM micrographs of fracture surfaces of the W–TiN composites. The composites added with 0.5 and 2 wt.% TiN are reported in Fig. 6(a) and (c). The grain size of W were refined from about 12.6 μm to 6.4 μm by the increasing TiN content from 0.5 wt.% to 4 wt.%, and the grain size distribution was homogeneous because of the mechanically mixed tungsten-based powders. As seen in Fig. 6(a), several small pores existed at the W grain boundary and the interface of W–TiN (the white rectangles in Fig. 6(a)), which could explain the low densification of W–0.5 wt.% TiN composites. In comparison, W–2 wt.% TiN showed less pores (in Fig. 6(d)). Based on research, the mode of fracture of pure W is typical intergranular, and the fracture appearance was straight. Fig. 6(b) illustrates the fracture surface of the 0.5 wt.% TiN composite, which shows a mix of intergranular fracture and scarce trans-granular ruptures. Fig. 6(c) shows that the trans-granular rupture increased with the addition of 2 wt.% TiN which were marked by black circles, and W/W intergranular and W/TiN intergranular fractures were observed. Several river patterns and a clear quasi cleavage facet of W grain fracture surface can be seen in Fig. 6(d). We speculated that with the addition of TiN particles, few cracks propagated along the W grain boundary, and the intergranular and transgranular fracture of TiN could be observed, resulting in the cracks changing the orientation of propagation that could absorb more energy. Several TiN particles were crushed or observed in the trans-granular fracture surface, and the fracture appearance was rough.

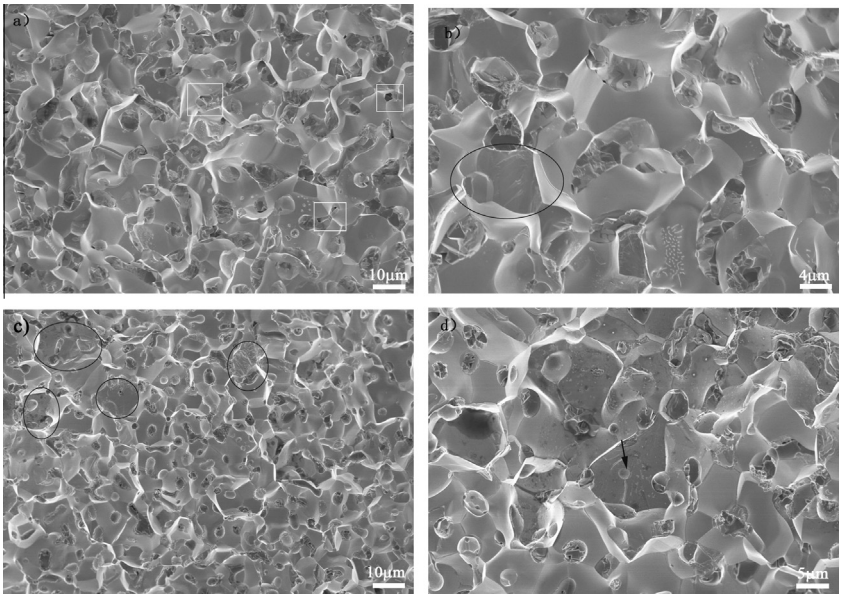

Fig. 6. SEM micrographs of fracture surfaces of W–TiN composites.

To characterize the features, TEM analysis was conducted on the W–2 wt.% TiN composites. The TEM bright field image is shown in Fig. 7(a). The image reveals that TiN particle exist at the W grain with a diameter of 0.2–0.4 μm. To clarify the phase of the particles, the selected area, diffraction pattern, and high-resolution TEM (HRTEM) were analyzed, as shown in Fig. 7(b)–(d), respectively. The TiN has a face-centered cubic structure with a lattice parameter of 0.24 nm along the zone axis of [1 1 0]. The tungsten matrix has a body-centered cubic structure with a lattice parameter of 0.15 nm along axis of [1 0 0], which was presented as the light color area in Fig. 7(a).

3.2.3. Thermal conductivity measurement

The thermal diffusivity of all samples was measured by LFA, and then the thermal conductivity was calculated as it is presented in Fig. 8. The thermal conductivity of W–TiN composites presented a nearly linear ascending trend with increasing temperature. The variation of thermal conductivity when the temperature increased further was not investigated. When the temperature increased from RT to 800 °C, the range of thermal conductivity of all samples was almost the same. Notably, the thermal conductivity decreased with the addition of TiN, because thermal conductivity was mainly ascribed to the W matrix [20]. However, the thermal conductivity

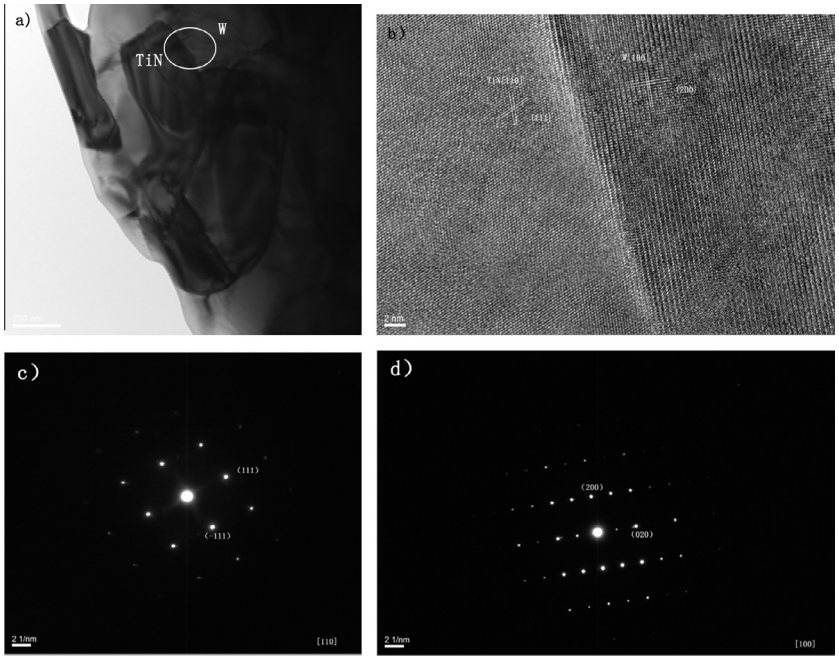

Fig. 7. TEM analysis of W–2 wt.% TiN composite: (a) bright field image, (b) the HRTEM of the W–TiN phase (c) the SAD pattern of TiN phase, and (d) the SAD pattern of W phase.

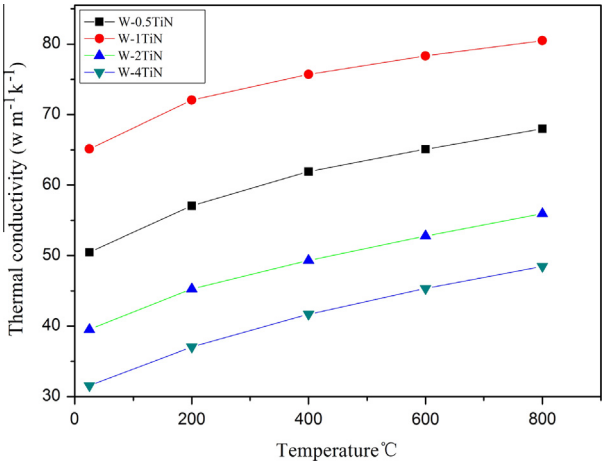

Fig. 8. The thermal conductivity curve of different ratio of W–TiN composites.

of W–1 wt.% TiN was better than others. To investigate the performance of these newly developed W–TiN alloys with SPS, all samples will be tested using H/He irradiation under fusion-relevant conditions in future.

4. Conclusion

W–(0.5, 1, 2, 4) wt.% TiN composites were prepared by spark plasma sintering. The TiN particles were dispersed uniformly, attributing a strengthening effect on the W matrix. The grain was refined, trans-granular fracture was achieved, and the micro-hardness was increased with the addition of TiN. The relative density and tensile strength strongly depended on the density of the sintered alloy materials, and the highest value was obtained for W–2 wt.% TiN composites, which had the highest density. The fracture surface of W–TiN possessed a mixed intergranular fracture, with few trans-granular rupture.

Acknowledgements

This paper was supported by National Magnetic Confinement Fusion Program with Grant No. 2014GB121001. The Fundamental Research Funds for the Central Universities No. 2012HGQC0032.

References

[1] V. Philipps, J. Nucl. Mater. 415 (2011) S2–S9.
[2] M. Rieth, S.L. Dudarev, S.M. Gonzalez de Vicente, J. Aktaa, T. Ahlgren, S. Antusch, J. Nucl. Mater. 432 (2013) 482–500.
[3] Y. Ishijima, H. Kurishita, K. Yubuta, H. Arakawa, M. Hasegawa, Y. Hiraoka, J. Nucl. Mater. 329–333 (2004) 775–779.
[4] M. Bhuyan, S.R. Mohanty, C.V.S. Rao, P.A. Rayjada, P.M. Raole, Appl. Surf. Sci. 264 (2013) 674–680.
[5] G. Peter, J. Nucl. Mater. 323 (2003) 304–312.
[6] V. Krsjak, S.H. Wei, S. Antusch, Y. Dai, J. Nucl. Mater. (2013). http://dx.doi.org/10.1016/j.jnucmat.2013.11.019.
[7] D. Rupp, R. Mönig, P. Gruber, S.M. Weygand, Int. J. Refract. Met. Hard. Mater. 28 (2010) 669–673.
[8] S. Wurster, B. Gludovatz, A. Hoffmann, R. Pippan, J. Nucl. Mater. 413 (2011) 166–176.
[9] M. Xia, Q.Z. Yan, L. Xu, H.Y. Guo, L.X. Zhu, C.C. Ge, J. Nucl. Mater. 434 (2013) 85–89.
[10] D.T. Blagoevaa, J. Opschoor, J.G. van der Laan, C. Sârbu, G. Pintsuk, M. Jong, T. Bakker, P. Ten Pierick, H. Nolles, J. Nucl. Mater. 442 (2013) S198–S203.
[11] B. Savoini, J. Martínez, A. Muñoz, M.A. Monge, R. Pareja, J. Nucl. Mater. 442 (2013) S229–S232.
[12] Y.W. Zhao, Y.J. Wang, L. Chen, Y. Zhou, G.M. Song, J.P. Li, Int. J. Refract. Met. Hard. Mater. 37 (2013) 40–44.
[13] N. Liu, Y.D. Xu, H. Li, G.H. Li, L.D. Zhang, J. Eur. Ceram. Soc. 22 (2002) 2409–2414.
[14] J.L. Li, K. Hu, Y. Zhou, Mater. Sci. Eng. A 326 (2002) 270–275.
[15] J. Deng, S. Li, Y. Xing, Y. Li, Surf. Eng. 30 (2014) 195–203.
[16] W. Setyawan, R.J. Kurtz, Scr. Mater. 66 (2012) 558–561.
[17] M.A. Yar, S. Wahlberg, H. Bergqvist, H.G. Salem, M. Johnsson, M. Muhammed, J. Nucl. Mater. 408 (2011) 129–135.
[18] Y.M. Kim, K.H. Lee, E.P. Kim, D.I. Cheong, S.H. Hon, Int. J. Refract. Met. Hard Mater. 27 (2009) 842–846.
[19] Z.M. Xie, R. Liu, Q.F. Fang, Y. Zhou, X.P. Wang, C.S. Liu, J. Nucl. Mater. 444 (2014) 175–180.
[20] Y. Jiang, J.F. Yang, Z. Zhuang, R. Liu, Y. Zhou, X.P. Wang, Q.F. Fang, J. Nucl. Mater. 433 (2013). pp. 499-454.